

Microstructural degradation of polycrystalline superalloys from oxidized carbides and implications on crack initiation

Kontis, Paraskevas; Collins, David M.; Wilkinson, Angus J.; Reed, Roger C.; Raabe, Dierk; Gault, Baptiste

DOI:

[10.1016/j.scriptamat.2017.12.028](https://doi.org/10.1016/j.scriptamat.2017.12.028)

License:

Creative Commons: Attribution-NonCommercial-NoDerivs (CC BY-NC-ND)

Document Version

Peer reviewed version

Citation for published version (Harvard):

Kontis, P, Collins, DM, Wilkinson, AJ, Reed, RC, Raabe, D & Gault, B 2018, 'Microstructural degradation of polycrystalline superalloys from oxidized carbides and implications on crack initiation', *Scripta Materialia*, vol. 147, pp. 59-63. <https://doi.org/10.1016/j.scriptamat.2017.12.028>

[Link to publication on Research at Birmingham portal](#)

Publisher Rights Statement:

DOI: 10.1016/j.scriptamat.2017.12.028

General rights

Unless a licence is specified above, all rights (including copyright and moral rights) in this document are retained by the authors and/or the copyright holders. The express permission of the copyright holder must be obtained for any use of this material other than for purposes permitted by law.

- Users may freely distribute the URL that is used to identify this publication.
- Users may download and/or print one copy of the publication from the University of Birmingham research portal for the purpose of private study or non-commercial research.
- User may use extracts from the document in line with the concept of 'fair dealing' under the Copyright, Designs and Patents Act 1988 (?)
- Users may not further distribute the material nor use it for the purposes of commercial gain.

Where a licence is displayed above, please note the terms and conditions of the licence govern your use of this document.

When citing, please reference the published version.

Take down policy

While the University of Birmingham exercises care and attention in making items available there are rare occasions when an item has been uploaded in error or has been deemed to be commercially or otherwise sensitive.

If you believe that this is the case for this document, please contact UBIRA@lists.bham.ac.uk providing details and we will remove access to the work immediately and investigate.

Microstructural degradation of polycrystalline superalloys from oxidized carbides and implications on crack initiation

Paraskevas Kontis^{a,*}, David M. Collins^b, Angus J. Wilkinson^c, Roger C. Reed^c, Dierk Raabe^a, Baptiste Gault^a

^a Max-Planck-Institut für Eisenforschung, Max-Planck-Str. 1, 40237 Düsseldorf, Germany.

^b School of Metallurgy and Materials, University of Birmingham, Edgbaston, B15 2TT, UK.

^c Department of Materials, University of Oxford, Parks Road, OX1 3PH, Oxford, UK.

Abstract

Surface connected carbides in a polycrystalline superalloy oxidised at 750 °C in air were studied as potential crack initiation sites. Lattice rotations measured in the γ/γ' grains using high-resolution electron backscatter diffraction enabled investigation of the plastic deformation induced solely by the oxidation of carbides. Dislocations were found to enhance γ' precipitate dissolution kinetics, resulting in soft recrystallized regions in the vicinity of the oxidised carbide with substantial compositional variation compared to the original γ/γ' microstructure. Ramifications of such deleterious oxidised carbides alongside soft recrystallized regions on the crack initiation life in superalloys are discussed.

Keywords: oxidised carbides, recrystallization, atom probe tomography, γ' dissolution, partial dislocation

MC-type carbides are known to serve as crack initiation sites under fatigue conditions at elevated temperatures in nickel-based superalloys by acting as stress concentration sites [1]. These inherently brittle particles cannot easily accommodate plastic deformation when subjected to high stresses, instead failing through fracture or decohesion from the γ/γ' microstructure. Micro-cracks originating from these loci may subsequently propagate [2]. When tested under complex stress and temperature cycles, the cracks may instead initiate in regions close to a free surface, originating from an oxidised MC carbide, and subsequently propagate within the bulk [3,4]. The products from the oxidation of the MC carbides result in their volume expansion, subsequently generating significant local plastic deformation [5]. Nevertheless, the exact mechanism for crack initiation by oxidised carbides is not well understood. For instance, it is not clear to what extent the localised plastic deformation occurs and whether the composition of the γ/γ' microstructure can be potentially altered.

Advanced characterisation techniques that offer spatially resolved quantification of deformation and composition now enable the mechanisms governing oxidised carbide failure to be investigated. Specifically, the combination of high angular resolution electron backscatter diffraction (HR-EBSD) permits characterisation of plasticity mechanisms and can be linked to composition measurements made using atom probe tomography (APT). From HR-EBSD, plastic deformation is inferred by quantifying the geometrically necessary dislocation (GND) density and distribution [6], based upon measurements of the lattice curvature and subsequent analysis of the Nye tensor [7]. This experimental method has previously been applied to superalloys to study the accumulation of GND fields near grain boundaries and non-metallic inclusions [8,9]. APT analysis of oxide particles and oxide scales from superalloys, oxide dispersion-strengthened ferritic alloys and steels have been successfully characterised giving accurate chemical composition data [10–15].

In this study, a polycrystalline superalloy IN792, commonly used in industrial gas turbines, was investigated. The chemical composition of the alloy is Ni-13.9Cr-8.8Co-1.1Mo-1.3W-7.6Al-4.9Ti-1.3Ta-0.4C-0.1B-0.012Zr (at.%). The carbon content was measured using a LECO CS444 analyser and for the other elements by inductively coupled plasma OES. Conventionally cast round bars with 20 mm diameter 20 mm of the material was supplied by Howmet. The as-cast bars were hot isostatically pressed (HIP) at 1195°C and 150MPa for 2h followed by solution heat treatment at 1121°C for 2h. The final stage of ageing was conducted at 850°C for 24h. Specimens were ground and polished with abrasive media to a 1 μ m (diamond suspension) finish (the surface roughness was not measured after the polishing stage) from a fully

heat-treated bar and were isothermally and statically exposed at 750°C for 50 hours under no external mechanical loading.

A dual column scanning electron microscope (SEM) and focused ion beam (FIB) Zeiss NVision 40 was used for surface observations, and HR-EBSD provided details on the plasticity mechanism in the vicinity of an oxidised MC carbide. A nickel layer was electrochemically deposited on the surface prior to preparation. The cross-section of the statically-exposed specimen was polished to a 0.04 μm colloidal silica finish. A JEOL 6500F field emission gun SEM operated at 20 kV and a current of ~ 14 nA, equipped with a TSL Digiview II Peltier-cooled charge coupled device was used. From a region-of-interest, a $14 \times 10 \mu\text{m}^2$ EBSD map was collected with 0.05 μm step size. EBSD patterns were recorded at full resolution (1000×1000 pixel) with 0.5 s exposure. The GND density was estimated using an in-house analysis method to quantify lattice curvature [6]. The areas of the GND map blanked are from oxidised and non-oxidised MC carbides for which the exact crystallographic information is unknown.

APT was used to investigate chemical variations between recrystallized grains and the deformed γ/γ' microstructure. Site-specific specimens were prepared from both regions, the MC carbide before and after oxidation, using a dual column SEM-FIB FEI Helios 600 following procedures described in Ref. [16], and analysed on a Cameca LEAP 5000 HR operated at a base temperature of 60 K in laser pulsing mode at 125 kHz, with 0.45 pJ pulse energy.

Figure 1a shows surface eruptions caused by the oxidation of MC carbides. Both inter- and intragranular carbides located close or connected to the surface oxidise, as shown in Figure 1b–c. Similar oxidised carbides in statically exposed samples have previously been reported [8,17,18]. A FIB cross-section of the intergranular oxidised carbide is shown in Figure 1d, in which the formation of pores due to the oxidation of the carbide is apparent. Pores are likely forming due to the outward formation of the oxide products towards the free surface. Pores formed after only 50 hours of static exposure at 750 °C in absence of external applied stress. Pores are known to serve as stress concentration sites where cracks can initiate in superalloys [19]. Thus, our observations give a first strong indication that cracks can primarily initiate within or in the vicinity of oxidised MC carbides.

Oxidation of the MC carbide was confirmed by APT, and Table 1 provides compositions of a MC carbide after heat treatment and one after isothermal static exposure in air at 750 °C for 50 hours. In the former, the MC carbide is Ti/Ta-rich, with low concentration of molybdenum and tungsten. After thermal exposure, the chemistry of the MC carbide was altered substantially. In Figure 1e, APT of an oxidised MC carbide shows two regions with different concentrations of Ti, Ta and O that likely correspond to TiO_2 and $(\text{Ti,Ta})_2\text{O}_5$. An elemental composition profile as a function of the distance from the $\text{TiO}_2/(\text{Ti,Ta})_2\text{O}_5$ interface (i.e. proxigram [20]) is presented in Figure 1f and the compositions is in Table 1. The oxygen concentration is lower than the expected stoichiometry, which can be ascribed either to a metastable state of the oxide or to an underestimation due to loss in detection [21,22]. Interestingly, the carbon content dramatically decreased from 47.40 at.% to only 2.3 at.% in the TiO_2 and 1.1 at.% in $(\text{Ti,Ta})_2\text{O}_5$, confirming oxidation. It is believed that carbon during the oxidation of the carbides contributes towards the formation of CO or CO_2 gas.

Substantial volume expansion due to the oxidation of MC carbides can result in localised plastic deformation [3,18], as confirmed here by HR-EBSD. A backscattered-electron micrograph near a partially oxidised MC carbide is shown in Figure 2a. The carbide is not entirely oxidised as observed by the distinct changes in contrast within the particle. The part of the carbide furthest from the surface appears unaffected. Recrystallization was observed around the oxidised carbide, as evidenced by the EBSD inverse pole figure map shown in Figure 2b. During exposure at elevated temperatures, and below the protective oxide scale at the surface, a γ' denuded zone forms, where recrystallization is often observed [10]. However, in our case, recrystallization is only present close to the oxidised carbide and not underneath the thin oxide layer that covers the entire surface. This implies that γ' dissolution and subsequent recrystallization is not directly related to the formation of a protective oxide scale, but instead is facilitated by dislocations produced by localised plasticity caused by volume expansion of the oxidised MC carbide.

In Figure 2c, the map reveals a high GND density area around the carbide, up to approximately 10^{15} – 10^{16} m^{-2} . This area extends more than $4 \mu\text{m}$ below the. Narrow veins of high GND density can be seen between recrystallized grains and the γ/γ' microstructure. Thermal strains were shown to extend up to approximately $1 \mu\text{m}$ around MC carbides in IN792 alloy after full heat treatment [4]. We hence believe that the high GND density shown in Figure 2c is mainly due to the volume expansion of the carbide during its oxidation. Due to the complex structure and combination of different oxides as shown in Figure 1e, calculation of the actual volume expansion is difficult. However, volume expansion of a Nb-rich MC carbide oxidizing to Nb_2O_5 was estimated to be over twofold and we can expect a similar factor herein [18]. Finally, a high GND density is observed in the γ channels between the non-dissolved γ' precipitates as indicated by the black arrows in Figure 2c.

An APT reconstruction from a specimen prepared from a region of the γ/γ' microstructure exhibiting a high GND density region is illustrated in Figure 3a. Previously, the enhancement of the kinetics of the dissolution of γ' precipitates due to a high dislocation density has been reported in a single crystal nickel-based superalloy [23]. Here, within a γ' precipitate, γ particles, which result from the applied heat treatment, appear [24,25]. Tubular features are also visible, and they correspond to elemental segregation to dislocations, as previously revealed by APT [26] and confirmed by correlative transmission electron microscopy / APT studies [27–31] or field ion microscopy [32]. Some dislocations appear as individual objects, some as pairs of partial dislocations. A cylindrical region-of-interest perpendicular to such a pair, positioned along arrow #1 in Figure 3a, reveals segregation of chromium and cobalt at the partial dislocations, whereas aluminium and titanium are depleted as shown in Figures 3b. Besides, nickel at the dislocations exhibits a slight depletion compared to γ' . These results for the pair of partials are consistent with recent reports, for two nickel-based superalloys, where this segregation of chromium and cobalt was interpreted as proof of pipe diffusion along the dislocations [33]. Pipe diffusion alters the local chemistry of the γ/γ' microstructure by leaching chromium and cobalt from the γ matrix thereby increasing nickel solubility, which eventually results in dissolution of γ' and the observed recrystallization [29]. Here, it is further shown that the partial dislocations exhibit different amount of chromium and cobalt segregation as shown in Figure 3b. Such difference could be related to different solute drag force associated with the leading and trailing partial dislocations [34]. However, extensive correlative TEM/APT are required to ascertain these preliminary observations.

The above observations also rationalises the composition of the recrystallized region, which differs substantially from the composition of the γ matrix. APT was performed in four critical locations around the oxidised carbide of Figure 2a, as denoted by yellow square boxes in Figure 4a. The composition of the γ matrix, obtained from the APT reconstruction shown in Figure 4b. In Figure 4c an APT dataset shows an interface between γ' and a region showing a substantial increase in nickel, from 45.7 at.% in the heat-treated γ matrix to 74.5 at.% in the recrystallized region. Besides, chromium dramatically decreases from 30.2 at.% to 8.3 at.%, whereas cobalt drops from 16.0 at.% to 10.4 at.%. The aluminium content was found unaltered. The composition is given in Table 2. Atom probe crystallography analysis [35] from this particular reconstruction reveals two sets of planes from the same directions on either side of the interface, which directly confirms the change in orientation between the γ' precipitate and a recrystallized grain.

The composition of the dataset shown in Figure 4d provides evidence of the general character of the substantial chemical alteration of the recrystallized grains to a new composition which differs from the γ matrix with a lower content of solution strengthening elements, thus it will be denoted as γ_R . Table 2 lists the measured compositions of γ_R across datasets indicates no significant variations across different datasets. In addition, it is expected from its composition, that γ_R is softer than the typical γ matrix allowing dislocations to move within the recrystallized regions more easily and would not oppose the initiation or propagation of cracks. That explains the high GND density within the recrystallized grains as shown in Figure 2c, and their accumulation towards the γ_R/γ' interface. This accumulation could also lead to the nucleation of cracks or the decohesion of the interface between the soft γ_R and the harder γ/γ' microstructure.

Finally, an APT reconstruction containing an interface between a γ' precipitate from the virgin microstructure and γ_R is shown in Figure 4e. Ti-rich nitrides were found to form at or near the γ_R/γ' interface

and within the γ' precipitate, with a composition given in Table 3. Their stoichiometry does not yet exactly correspond to TiN nitrides often observed in nickel-based superalloys [36], which could be due to the thermal exposure too short to complete the formation of TiN. Similar nitrides were observed in other nickel-based superalloys during oxidation of MC carbides [37]. The presence of brittle nitrides at that interface can also facilitate crack initiation and propagation.

The combined presence of an oxidised carbide and soft recrystallized grains will be deleterious for the crack initiation life of polycrystalline nickel-based superalloys. In the case of external applied loads, micro-cracks can initiate from the sometimes porous oxide at the surface, and then propagate within the bulk [38,39]. For instance, it was shown under OP-thermal-mechanical fatigue conditions that cracks initiate from oxidised MC carbides and propagate in a transgranular manner in single-notched cylindrical specimens of IN792 [4]. The strong accumulation of defects induced by the volume expansion of the oxidised carbide within the softer, finer microstructure in its vicinity is also likely to facilitate crack nucleation. The number of crack initiation sites will scale with the volume fraction and the shape of precipitated MC carbide, which need to be controlled: careful selection of the carbon content in superalloys can improve the crack initiation life under fatigue conditions. The shape of the MC carbides may also influence the crack initiation life. Intragranular script-type MC carbides can serve as sharp oxide intrusions from which cracks can propagate more rapidly. A combination of casting conditions and careful selection of compositions that control MC carbides formation can result in more desirable blocky MC carbides [40,41]. The chemistry of the MC carbide impacts its oxidation behaviour and lower the crack initiation life of superalloys containing Nb-rich MC carbides that oxidise more easily than a Ti-rich MC carbide under the same exposure conditions, based on the free energy of formation of their corresponding oxides.

In summary, our findings provide new insights on the crack initiation mechanism caused by the oxidation of MC carbides in polycrystalline superalloys. HR-EBSD confirmed that the volume expansion of, often porous, oxidised carbides connected to the surface results in high GND density regions. In such regions, the dissolution kinetics of the γ' precipitates is enhanced via pipe diffusion of chromium and cobalt at dislocations. As a consequence, soft recrystallized regions with limited amounts of solute strengthening elements form in the vicinity of oxidised MC carbides. The concurrent presence of hard but porous oxidised MC carbides and soft recrystallized γ_R regions will dramatically decrease the crack initiation life of polycrystalline superalloys. Thus, the volume fraction of MC carbides needs to be considered with extreme care during the design of new polycrystalline superalloys.

Acknowledgements

The authors thank Siemens Industrial Turbomachinery AB, Sweden for the provision of the material. Uwe Tezins and Andreas Sturm are also acknowledged for their support on APT experiments.

References

- [1] P.S. Karamched, A.J. Wilkinson, *Acta Mater.* 59 (2011) 263–272.
- [2] L.H. Rettberg, T.M. Pollock, *Acta Mater.* 73 (2014) 287–297.
- [3] A. Pineau, D.L. McDowell, E.P. Busso, S.D. Antolovich, *Acta Mater.* 107 (2016) 484–507.
- [4] P. Kontis, D.M. Collins, S. Johansson, A.J. Wilkinson, J.J. Moverare, R.C. Reed, in: *Superalloys 2016 13th Int. Symp.*, 2016, pp. 763–772.
- [5] P.A.S. Reed, *Mater. Sci. Technol.* 25 (2009) 258–270.
- [6] A.J. Wilkinson, D. Randman, *Philos. Mag.* 90 (2010) 1159–1177.
- [7] J. Nye, *Acta Metall.* 1 (1953) 153–162.
- [8] P. Kontis, E. Alabort, D. Barba, D.M. Collins, A.J. Wilkinson, R.C. Reed, *Acta Mater.* 124 (2017) 489–500.
- [9] T. Zhang, D.M. Collins, F.P.E. Dunne, B.A. Shollock, *Acta Mater.* 80 (2014) 25–38.
- [10] S. Pedrazzini, D.J. Child, G. West, S.S. Doak, M.C. Hardy, M.P. Moody, P.A.J. Bagot, *Scr. Mater.* 113 (2016) 51–54.
- [11] P. Kontis, S. Pedrazzini, Y. Gong, P.A.J. Bagot, M.P. Moody, R.C. Reed, *Scr. Mater.* 127 (2017) 156–159.

- [12] D.J. Larson, P.J. Maziasz, I.-S. Kim, K. Miyahara, *Scr. Mater.* 44 (2001) 359–364.
- [13] L. Viskari, M. Hörnqvist, K.L. Moore, Y. Cao, K. Stiller, *Acta Mater.* 61 (2013) 3630–3639.
- [14] K. Stiller, L. Viskari, G. Sundell, F. Liu, M. Thuvander, H.-O. Andréén, D.J. Larson, T. Prosa, D. Reinhard, *Oxid. Met.* 79 (2013) 227–238.
- [15] Y. Gong, D.J. Young, P. Kontis, Y.L. Chiu, H. Larsson, A. Shin, J.M. Pearson, M.P. Moody, R.C. Reed, *Acta Mater.* 130 (2017) 361–374.
- [16] K. Thompson, D. Lawrence, D.J. Larson, J.D. Olson, T.F. Kelly, B. Gorman, *Ultramicroscopy* 107 (2007) 131–139.
- [17] L. Mataveli Suave, J. Cormier, P. Villechaise, D. Bertheau, G. Benoit, F. Mauget, G. Cailletaud, L. Marcin, in: *Superalloys 2016 13th Int. Symp.*, 2016, pp. 747–756.
- [18] T. Connolly, P.A.S. Reed, M.J. Starink, *Mater. Sci. Eng. A* 340 (2003) 139–154.
- [19] H.T. Pang, P.A.S. Reed, *Mater. Sci. Eng. A* 448 (2007) 67–79.
- [20] O.C. Hellman, J.A. Vandenbroucke, J. Rüsing, D. Isheim, D.N. Seidman, *Microsc. Microanal.* 6 (2000) 437–444.
- [21] E.A. Marquis, N.A. Yahya, D.J. Larson, M.K. Miller, R.I. Todd, *Mater. Today* 13 (2010) 34–36.
- [22] B. Gault, D.W. Saxey, M.W. Ashton, S.B. Sinnott, A.N. Chieramonti, M.P. Moody, D.K. Schreiber, *New J. Phys.* 18 (2016) 33031.
- [23] R. Giraud, Z. Hervier, J. Cormier, G. Saint-Martin, F. Hamon, X. Milhet, J. Mendez, *Metall. Mater. Trans. A Phys. Metall. Mater. Sci.* 44 (2013) 131–146.
- [24] M. Segersäll, P. Kontis, S. Pedrazzini, P.A.J. Bagot, M.P. Moody, J.J. Moverare, R.C. Reed, *Acta Mater.* 95 (2015) 456–467.
- [25] V. Yardley, I. Povstugar, P.-P. Choi, D. Raabe, A.B. Parsa, A. Kostka, C. Somsen, A. Dlouhy, K. Neuking, E.P. George, G. Eggeler, *Adv. Eng. Mater.* 18 (2016) 1556–1567.
- [26] D. Blavette, E. Cadel, A. Fraczkeiwicz, A. Menand, *Science* 286 (1999) 2317–2319.
- [27] B. Gault, M.P. Moody, J.M. Cairney, S.P. Ringer, *Mater. Today* 15 (2012) 378–386.
- [28] G.D.W. Smith, D. Hudson, P.D. Styman, C.A. Williams, *Philos. Mag.* 93 (2013) 3726–3740.
- [29] M. Kuzmina, M. Herbig, D. Ponge, S. Sandlobes, D. Raabe, *Science* 349 (2015) 1080–1083.
- [30] K.S. Chan, *Metall. Mater. Trans. A Phys. Metall. Mater. Sci.* 46 (2015) 2491–2505.
- [31] A. Kwiatkowski da Silva, G. Leyson, M. Kuzmina, D. Ponge, M. Herbig, S. Sandlöbes, B. Gault, J. Neugebauer, D. Raabe, *Acta Mater.* 124 (2017) 305–315.
- [32] J. Wilde, A. Cerezo, G.D.W. Smith, *Scr. Mater.* 43 (2000) 39–48.
- [33] P. Kontis, Z. Li, D.M. Collins, J. Cormier, D. Raabe, B. Gault, *Scr. Mater.* 145 (2018) 76–80.
- [34] R.B. Sills, W. Cai, *Philos. Mag.* 96 (2016) 895–921.
- [35] B. Gault, M.P. Moody, J.M. Cairney, S.P. Ringer, *Mater. Today* 15 (2012).
- [36] S. Pedrazzini, E.S. Kiseeva, R. Escoube, H.M. Gardner, J.O. Douglas, A. Radecka, P.M. Mignanelli, G.M. Hughes, G. Chapman, P.D. Edmondson, H.J. Stone, D. de Lille, P.A.J. Bagot, *Oxid. Met.* (2017) 1–20.
- [37] J. Litz, A. Rahmel, M. Schorr, *Oxid. Met.* 30 (1988) 95–105.
- [38] Z.W. Huang, Z.G. Wang, S.J. Zhu, F.H. Yuan, F.G. Wang, *Mater. Sci. Eng. A* 432 (2006) 308–316.
- [39] R.A. Kupkovits, R.W. Neu, *Int. J. Fatigue* 32 (2010) 1330–1342.
- [40] J. Chen, J.H. Lee, C.Y. Jo, S.J. Choe, Y.T. Lee, *Mater. Sci. Eng. A* 247 (1998) 113–125.
- [41] Q.Z. Chen, N. Jones, D.M. Knowles, *Acta Mater.* 50 (2002) 1095–1112.

Figures

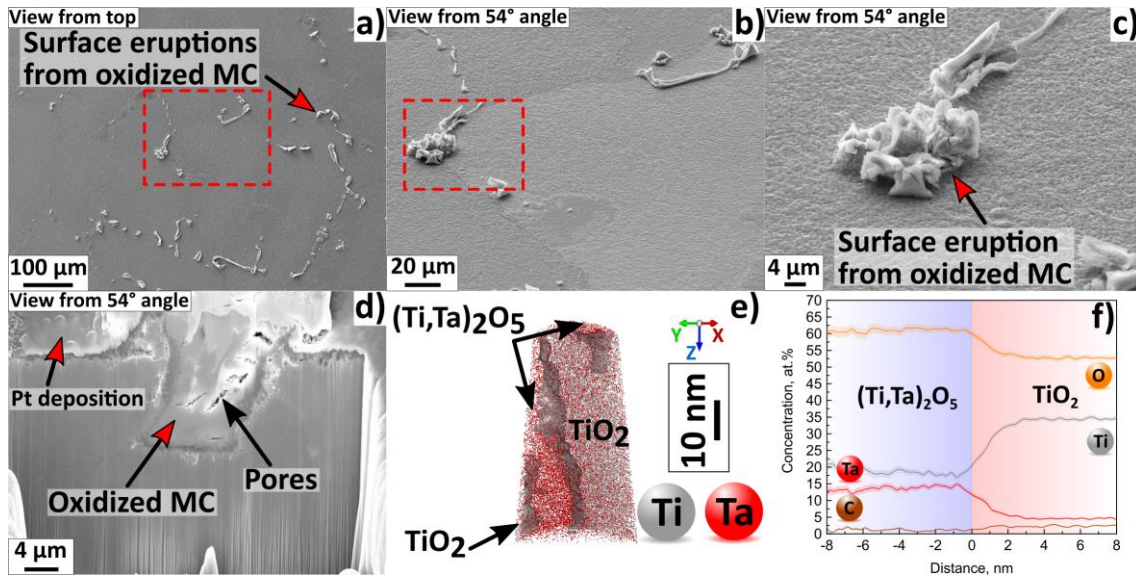


Figure 1: Secondary SEM micrographs showing: a) top view of surface eruptions from oxidised MC carbides, b) intergranular and intragranular oxidised MC carbides as denoted by the red dashed box in Figure 1a shown with the sample tilted 54° normal to the electron beam c) detail of surface eruption from the intergranular oxidised MC carbide denoted by the red dashed box in Figure 1b d) FIB section normal to the sample surface showing the oxidised MC carbide from Figure 1c within the bulk and the formation of pores, e) APT reconstruction from an oxidised MC carbide showing with an iso-concentration surface at 23.0 at.% Ti, TiO₂/(Ti,Ta)₂O₅ interfaces. f) Concentration profile across the TiO₂/(Ti,Ta)₂O₅ interface. Error bars are shown as lines filled with colour and correspond to the 2σ counting error.

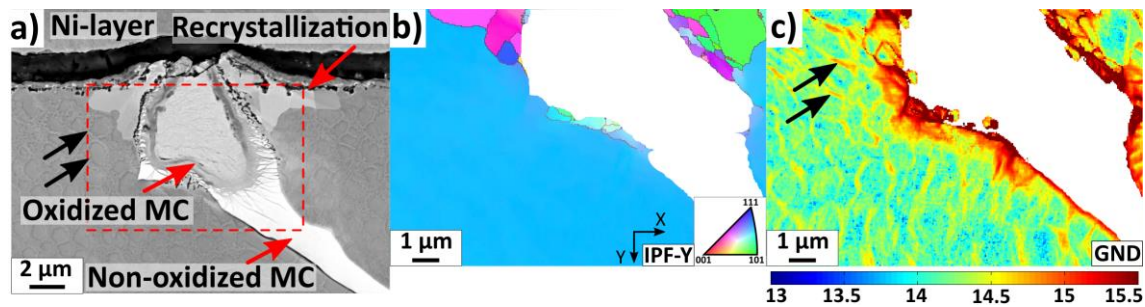


Figure 2: a) Backscattered SEM image showing recrystallization in the vicinity of an intragranular oxidised MC carbide connected to the surface, b) EBSD inverse pole figure (IPF) map (reference vector in vertical Y direction) confirming the recrystallization. The IPF map corresponds to the area denoted by the red dashed box and c) HR-EBSD strain map from the region as denoted in Figure 2a by the red dashed box, showing the GND density map with the scale bar in log₁₀ scale of dislocation lines m⁻². Black arrows in Figure 2c indicate high GND density in γ channels and correspond to the black arrows in Figure 2a.

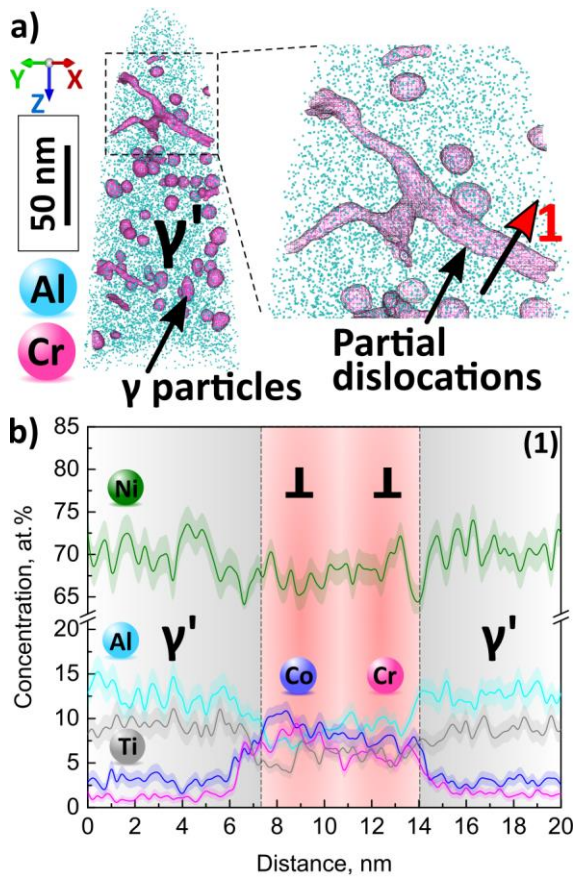


Figure 3: a) APT reconstruction from a high GND density γ/γ' region next to an oxidised MC carbide, showing with an iso-concentration surface at 4.0 at.% Cr dislocations and γ precipitates within the γ' precipitate, alongside detail of the APT reconstruction showing the position of the cylindrical region of interest perpendicular to a pair of partial dislocations (arrow #1). b) 1D concentration profile perpendicular to the denoted pair of partial dislocations in Figure 3a (arrow #1). Error bars are shown as lines filled with colour and correspond to the 2σ counting error.

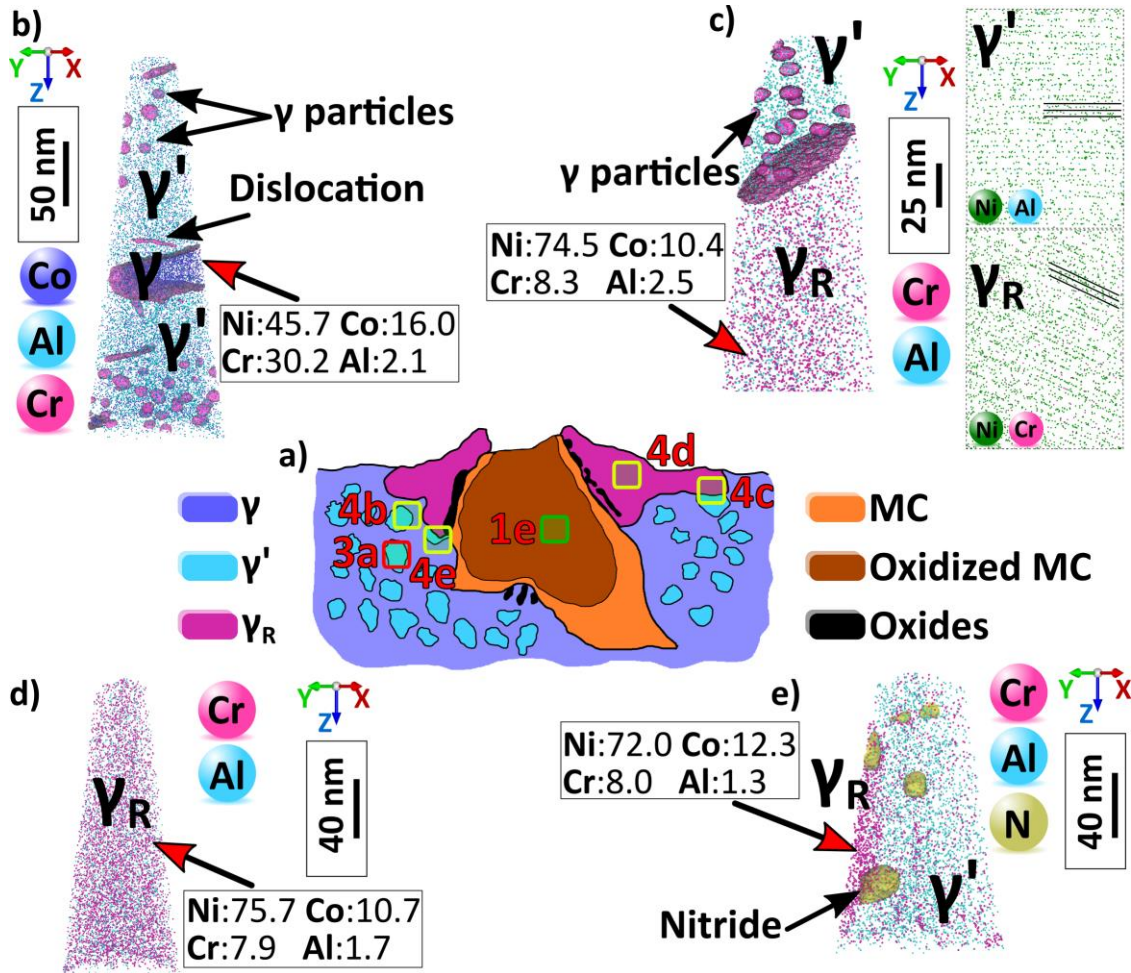


Figure 4: a) Descriptive schematic illustration (centre) of the oxidised carbide from Figure 2a. b) APT reconstruction from a high GND density γ/γ' region, showing with an iso-concentration surface at 3.0 at.% Cr γ/γ' interfaces, dislocations and γ precipitates within the γ' precipitate. c) APT reconstruction showing with an iso-concentration surface at 3.0 at.% Cr a γ/γ_R interface, γ precipitates within the γ' precipitate and analysis of the crystallographic planes perpendicular to the analysis direction of γ/γ_R . d) APT reconstruction within a γ_R recrystallized grain and e) APT reconstruction showing a γ_R/γ' interface and nitrides at the γ_R/γ' interface and within the γ' precipitate are shown with an iso-concentration surface at 2.7 at.% N. The yellow square boxes denote the location of each atom probe reconstruction in Figure 4, whereas the green and red boxes denote the location of the atom probe datasets from Figures 1e and 3a, respectively.

Tables

Table 1: Summary of chemical compositions of the MC carbide after full heat treatment and after isothermal exposure in air at 750 °C for 50 hours as measured by atom probe tomography (at.%).

	C	Ni	Cr	Al	Ti	Ta	Mo	W	O
MC	47.4±0.02	0.0	0.5±0.01	0.0	30.0±0.04	18.5±0.03	1.7±0.01	1.6±0.01	0.00
MC/TiO ₂	2.3±0.01	1.7±0.08	1.0±0.06	1.0±0.07	34.1±0.09	4.7±0.06	0.0	1.2±0.03	52.9±0.45
MC/(Ti,Ta) ₂ O ₅	1.1±0.01	0.4±0.11	0.3±0.06	0.4±0.05	18.5±0.07	13.7±0.05	0.0	3.5±0.01	61.3±0.17

Table 2: Summary of chemical compositions of the γ_R recrystallized regions and the γ matrix after isothermal exposure in air at 750 °C for 50 hours as measured by atom probe tomography, corresponding to APT reconstructions in Figure 4 (at.%).

	Ni	Co	Cr	Al	Mo	W	Ti	Ta
γ (4b)	45.7±0.09	16.0±0.07	30.2±0.07	2.1±0.02	2.3±0.02	1.2±0.03	1.7±0.01	0.1±0.01
γ_R (4c)	74.5±0.02	10.4±0.01	8.3±0.01	2.5±0.01	1.2±0.01	1.0±0.01	1.0±0.01	0.6±0.01
γ_R (4d)	75.7±0.01	10.7±0.01	7.9±0.01	1.7±0.01	1.3±0.01	1.0±0.01	0.6±0.01	0.6±0.01
γ_R (4e)	72.0±0.06	12.3±0.04	8.0±0.03	1.3±0.01	1.0±0.01	2.3±0.03	1.3±0.01	1.0±0.01

Table 3: Summary of the chemical compositions of the nitrides observed after isothermal exposure in air at 750 °C for 50 hours as measured by atom probe tomography (at.%).

	Ti	Cr	Mo	C	Ta	Ni	N
Nitride in γ'	45.1±0.41	9.6±0.29	1.9±0.02	1.4±0.16	0.6±0.07	0.6±0.33	39.8±0.23
Nitride in γ_R/γ' interface	45.2±0.28	9.7±0.18	2.0±0.04	1.5±0.09	0.8±0.06	0.5±0.09	36.9±0.31